KOM
CORROSION AND MATERIAL PROTECTION JOURNAL

ORIGINAL ARTICLE

sciendo

Investigations on the texture and corrosion characteristics of AA5083 alloy reinforced with CeO_2 by friction stir processing

Arun Prakash D. [1], *Annirut P.* [1], *Lokesh Kumar A.*[1], *Phanindra Saketh Ch.*[1], *Vaira Vignesh R.*[1], *Padmanaban R.*[1], *Baghad A.*[2]

[1] **Department of Mechanical Engineering, Amrita School of Engineering, Coimbatore, Amrita Vishwa Vidyapeetham, India**

[2] **ICAM, Site de Grand Paris Sud, 77127 Lieusaint, France**

E-mail: r_vairavignesh@cb.amrita.edu, dr_padmanaban@cb.amrita.edu

AA5083 alloy exhibits favorable resistance to corrosion and welding characteristics, making it attractive for application in the marine environment. However, pitting and intergranular corrosion of AA5083 is still troublesome. This study investigates the corrosion resistance and texture evolution of friction stir processed AA5083 alloy with Cerium Oxide (CeO_2) as reinforcement. The FSP trials were performed by varying the process parameters: tool rotation speed (TRS), tool traverse speed (TTS), and a constant shoulder diameter (SD). The fabricated surface composite (FSC) specimens were subjected to microstructure, microhardness, intergranular corrosion, and electrochemical corrosion analysis. The specimens were subjected to advanced analytical instruments such as TEM, EBSD, and XRD to study the microstructure and texture evolution. The results showed that the corrosion of AA5083 alloy in the saline environment is highly suppressed by reinforcing it with cerium oxide (CeO_2) using friction stir processing, as it acted as a good corrosion inhibitor.

INTRODUCTION

Marine and structural applications require high strength, lightweight, and corrosion-resistant materials. Pure aluminum (Al) is a versatile metal recognized as lightweight and corrosion-resistant. However, the low strength and extreme flexibility constraints its usage in structural applications. But the properties of Al could be improved significantly through alloying with Mg, Cu, or Zn. One of the most significant alloys in the Al–Mg alloy system used in marine applications such as submarines, boats, and ships include AA5083 alloy [1].

The limitations of AA5083 alloy in the marine environment include corrosion predominantly along the grain boundaries. Intergranular corrosion heavily deteriorates the strength of the alloy, which could be suppressed by coating, adding corrosion inhibitors, or compositing with other materials. Surface composite can be an added advantage to combat corrosion in the marine environment, as delamination of coatings and the addition of corrosion inhibitors become out of work. Hence, surface modification techniques could be used to change the surface properties of AA5083 alloy through microstructural changes.

The surface composites can easily be fabricated by Friction Stir Processing (FSP), a solid-state processing technique. FSP is advantageous for aluminum alloys, as the absence of liquidation of the material avoids the rapid oxidation of aluminum (Al_2O_3) during the processing. Also, unnecessary interaction with the external environment is reduced in this process. It works on the premise of plunging a spinning tool with a specifically designed pin and shoulder into the material and traversing it over the surface, as indicated in Figure 1. The main microstructural changes (grain refinement) occur in the stir zone (SZ) because of intense plastic deformation and dynamic recrystallization depending on tool rotation speed (TRS), tool traverse speed (TTS), and tool geometry [1, 2]. Furthermore, the FSP can produce composites by introducing reinforcements by making holes or grooves on the material surface.

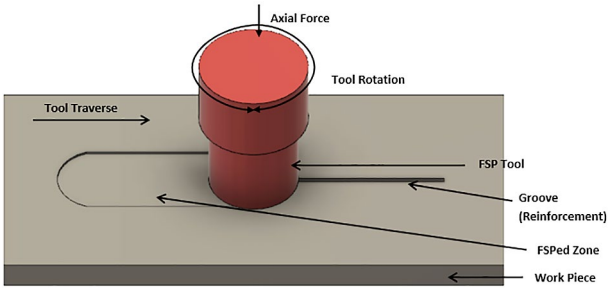

Fig. 1. Schematic representation of friction stir processing

A groove drilled holes or a cover plate are all popular ways of reinforcing particles for manufacturing surface composites. Because previous studies revealed a more homogenous dispersion of reinforcement particles, adding reinforcement through grooves would be helpful. The potential reinforcements for aluminum alloys could be SiC, Al_2O_3, WC, Si_3N_4, BN, TiO_2, TiC, and $LnCl_3$. To strengthen the corrosion resistance of the AA5083 alloy, cerium oxide reinforcement can be added to the grooves. Cerium ions create insoluble hydroxides, allowing them to operate as efficient cathodic inhibitors while causing minimal environmental impact. As a result, strengthening AA5083 alloy with CeO_2 does not promote intergranular corrosion. The potential scope of using CeO_2 to protect aluminum alloys against corrosion in maritime conditions is seldom discussed in the open literature [2-4]. Amra et al. [3] investigated the mechanical characteristics and corrosion behavior of AA5083 alloy reinforced by different volume ratios of CeO_2 and SiC. It was conclusive that AA5083-CeO_2 had an increased passivation range and good corrosion resistance, and AA5083-SiC had increased hardness. Sadegh et al. [1] investigated the corrosion sensitivity of friction stir-processed AA5083 aluminum alloy. The results proved that the passivation range of FSPed material was higher than the base material, making it an effective way for the improvement of corrosion resistance of the aluminum alloy.

Petru et al. [2] investigated the effect of annealing time and temperature on the intergranular corrosion (IGC) of AA5083-H321 aluminum alloy. It was conclusive that slow cooling favors the formation of discontinuous intermetallic particles along boundaries, ensuring high resistance to IGC. Chuajun et al. [4] investigated the mechanical properties of AA5083 in different tempers at low temperatures. It was found that temper-H321 alloy had better mechanical properties, such as Young's modulus, bend strength & impact properties, than other tempers.

Vaira Vignesh et al. [5] studied the microstructure and IGC susceptibility of friction stir processed AA5083 alloy. It was observed that FSPed AA5083 resulted in the minimal dissolution of secondary phase particles and dispersion in the matrix, thereby reducing the IGC susceptibility and mass loss in the material. Prabhakar et al. [6] investigated the grain size and corrosion rate of AA5083 alloy reinforced with fly ash by friction stir processing. The FSPed specimen had a reduced corrosion rate of 0.015 mm/year compared to the corrosion rate of the as-received AA5083 alloy (0.35 mm/year). The increase in corrosion rate could be attributed to the micro galvanic coupling phenomenon.

Vikram Kumar et al. [7] investigated the effect of the volume fraction of SiC and CNTs particles on the microstructure and mechanical properties of the surface composite of AA5083 alloy. It was observed that AA 5083-CNTs had better grain refinement, and AA5083-SiC had increased hardness than other combinations of reinforcements. Behnagh et al. [8]investigated the microstructural evolution and hardness of friction stir-processed AA5083 alloy. The intense plastic deformation and frictional heating lead to a recrystallized fine grain structure with equiaxed grains in grain size in various regions: the stir zone – fine and equiaxed, thermomechanically affected zone – elongated grains. Hence, the FSPed material had refined grains and maximum hardness.

Ashraf et al. [9] discussed the corrosion behavior of AA5083 alloy that was reinforced with finely powdered CeO_2 (0% to 1% of concentration) through the stir casting technique. CeO_2 particles acted as the cathodic zones, suppressing corrosion of the AA5083 alloy. Thus, the AA5083-0.2CeO_2 composite had 39% more corrosion inhibition efficiency in the salt spray test. Vivek et al. [10] studied the effect of tool rotational speed on microstructure and mechanical properties of FSPed AA5083 alloy reinforced with Fe-40 wt% Al. The dynamic recrystallization resulted in a peak microhardness of 123.3 HV (66.2% higher than the base material) and maximum tensile strength of 225.8 MPa (17.8% lower than the base material).

Ehab et al. [11] investigated the microstructural evolution and mechanical properties of friction stir processed AA5083 alloy. FSP transformed the elongated grains into fine and equiaxed grains with an average grain size of 1.6 μm and high-angle grain boundaries at the nugget zone. Huang et al.[12] studied the effect of microstructural features on the tensile properties of friction stir-processed AA5083.The as-received AA5083 alloy specimen had coarse grains, whereas the FSPed AA5083 alloy had fine equiaxed grains, sub-boundaries, and a high density of fine particles. The FSPed specimen had refined grains with a reduced grain size and high tensile strength higher than the base material.

Garcia et al. [13] investigated the microstructural homogeneity of FSPed AA5083 alloy fabricated by different primary processing routes, such as rolled, cast, and extruded. Due to large deformations and temperature, fine refinement of grains occurred due to dynamic crystallization. The combination of continuous cast AA5083 alloy (under twin rolled conditions) and FSP proved to be the best from the point of view of superplastic properties. Hayashi et al. [14] investigated the superplasticity and grain refinement of friction stir processed as-cast AA5083 alloy. FSP refined the grain size within the stir zone and redistributed the coarse Al_6Mn phase in the AA5083 alloy. The superplastic ductility of the material was improved than that of the base material.

Ziyaur et al. [15] investigated the effect on the surface properties of AA5083 alloy that was reinforced with titanium (Ti) and silicon carbide (SiC) in a 10:3

ratio through FSP. The microstructure of processed regions significantly varied grain size in various regions: stir zone – fine and equiaxed, thermo-mechanically affected zone – elongated grains. The highest hardness of 124.5 HV was obtained in the FSPed specimen at TRS of 355 rpm, TTS of 63 mm/min, and tool shoulder diameter of 17 mm.

Mehdi et al. [16] investigated the effect of processing parameters on the fabrication of AA5083-Cu composites through friction stir processing. The fabrication of the specimen reduced the grain size and increased the microhardness and tensile strength. Khalil et al. [17] investigated the effect on the microstructure and wear behavior of AA5083 alloy that was reinforced with different CeO_2 and SiC reinforcement volume ratios. The highest hardness found in the AA5083 alloy with SiC reinforcement was 117HV (1.5 times hard than the base metal AA5083 alloy), with a 50% improvement from the base alloy.

Sabitha et al. [18] investigated the synthesis and characterization of SiC/Al_2O_3 Reinforced AA5083 Metal Matrix Composite by Friction Stir Processing. It was conclusive that the microhardness for both samples was decreased by 40%, and the tensile strength for both samples was decreased by 54% and 42% compared to the base metal AA5083 alloy. This clearly shows that the average elongation percentage was increased than the AA5083 alloy. Omolayo et al. [19] investigated the influence of reinforcements B_4C/SiC/TiC in friction stir processing of AA5083 alloy. The microhardness was increased by 1.7 times, tensile strength was increased by 14.6%, and wear rate was decreased by 45.2% compared to the AA5083 alloy.

The effect of reinforcement of CeO_2 on the texture evolution of AA5083 alloy was seldom discussed in the open literature. In this study, the FSP was done on wrought AA5083 alloy plates with CeO_2 reinforcements by the selected FSP parameters. The FSP parameters considered were TRS, TTS, and SD. The FSPed workpieces will be characterized for texture, hardness, corrosion resistance, and intergranular corrosion resistance. The effects of FSP and the reinforcement on the base material AA5083 alloy concerning the corrosion resistance and texture evolution were investigated.

This work applied FSP on AA5083 alloy plates with CeO_2 reinforcements to obtain an AA5083-CeO_2 surface composite. The influence of CeO_2 reinforcement on the microstructure, texture, and corrosion characteristics of AA5083 alloy has not been explored in the open literature. AA5083 alloy-based surface composite with CeO_2 as reinforcements were fabricated by friction stir processing. The microstructure was analyzed using a scanning electron microscope, energy-dispersive X-ray spectroscope, electron back-scattered diffraction, and transmission electron microscope. The texture evolution of the material was analyzed by electron back-scattered diffraction. Corrosion characteristics of the material were evaluated by intergranular corrosion and electrochemical corrosion tests. A detailed analysis of the correlation of microstructure and texture with the corrosion properties of the material was presented.

MATERIALS AND METHODS

Materials

Wrought AA5083 alloy plates having a thickness of 6 mm were machined into the workpieces of dimension 150 × 50 mm by hydraulic shear cutting machine. The composition of AA5083 alloy is shown in Table 1. The plates were then grooved for 1 mm depth × 1 mm width × 100 mm length using a numerically controlled vertical milling center. The faces of the plates were deburred and paralleled to ensure good clamping in fixtures. The fabricated workpieces were cleaned and degreased with acetone before initiating the FSP process. The reinforcement was Cerium Oxide (CeO_2), a rare-earth metal oxide that had an average particle of size 30 μm and 99.9% purity was used.

Methodology

Friction stir processing

The FSP process parameters considered in the study are Tool Rotation Speed (TRS), Tool Traverse Speed (TTS), and the number of passes. The grooved workpiece was degreased and cleaned using acetone. The grooves were then filled with CeO_2 as reinforcement particles. The friction stir processing trials were performed using the dedicated friction stir welding setup in Amrita Vishwa Vidyapeetham, Coimbatore. The surface composite of AA5083 alloy was fabricated using sealing and FSP tools made of high-chromium high-carbon steel (HCHCr). A sealing pass was performed to avoid the scattering of reinforcement particles in the course of the FSP trial. The sealing pass was performed utilizing a sealing tool devoid of the pin and a shoulder diameter of 18 mm. The geometric features of the FSP tool include a shoulder

Tab. 1. Composition of aluminum alloy AA5083 (Base Material)

Element	Mg	Si	Mn	Cr	Fe	Cu	Zn	Ti	Al
Composition (wt%)	4.53	0.12	0.60	0.087	0.26	0.10	0.048	0.010	Remaining

diameter of 18 mm, a pin diameter of 5 mm, and a pin height of 5 mm. The friction stir process parameters, such as TRS and TTS, were varied in three levels, as shown in Table 2.

Tab. 2. Chosen levels of FSP process parameters

Trial number	TRS (rpm)	TTS (mm min^{-1})	Number of passes
FSP01	750	20	1, 2
FSP02	750	40	1, 2
FSP03	900	20	1
FSP04	350	20	1

Microstructure

The FSPed specimens having dimensions 10 × 5 × × 6 mm were cut from the fabricated surface composite. The specimens were prepared and polished as per the standard metallographic techniques and the standard ASTM E3-11 norms. The surface polished specimen was electropolished for 11 seconds at 9 volts using an etchant, a mixture of 80% ethanol and 20% perchloric acid. The etched specimens were observed under a high-resolution scanning electron microscope (Make: FEI Model: Quanta 200).

Crystallographic texture

The FSC specimens having dimensions 10 × 5 × × 6 mm were cut out from the fabricated surface composite. The specimens were then prepared, polished, and etched per the protocols described in the microstructure section. Texture analysis (grain size, crystallographic orientation, positions and intensities of specific crystallographic orientations, and misorientation angle) was performed using an electron back-scattered diffraction (EBSD) technique using TSL-EDX OIM system that was coupled with the high-resolution scanning electron microscope.

Microhardness

The microhardness of the base material and FSC were measured using Vicker's microhardness tester. The microhardness was evaluated by applying an axial load of 9.80 N (1 kg) for 20 s. The microhardness was measured at a sequential distance of 1 mm. The value of the average microhardness of ten measurements was reported.

Intergranular corrosion susceptibility test

The IGC of the base material and the FSC were evaluated through the nitric acid mass loss test (NAMLT) per the norms of ASTM G67-13. The processed 10 × 10 mm specimens were cut from the fabricated surface composite. The specimens were then polished as per the standard metallographic polishing technique. The polished specimens were immersed in boiling 5% sodium hydroxide (NaOH) to remove the surface contaminants. Then, the specimens were rinsed sequentially in distilled water, dipped in nitric acid (HNO_3), rinsed again in distilled water to remove the surface impurities, and dried in hot air. The specimen weights were measured using a digital weighing balance with a least count of 0.0001 g. The area of the specimens was determined using the dimensions, which were measured using a digital vernier caliper of least count 0.01 mm. The specimens were placed facing edges against the walls of the container. The setup was left undisturbed for 24 hours. Later, the specimen was rinsed in distilled water. The wobbly corrosion products were removed using a stiff plastic brush. The mass lost per unit area of the specimens after the IGC test was calculated using the equation (1).

$$\text{Mass Loss per unit area (mg cm}^{-2}\text{)}, M_a = \frac{m_1 - m_2}{A} \quad (1)$$

where, m_1 is the mass of the specimen before NAMLT, m_2 is the mass of the specimen after NAMLT, and A is the surface area of the specimen.

Electrochemical corrosion

The specimens for the corrosion testing measuring 150 × 50 × 5 mm were prepared from both the base material and FSC specimen. The insulation tapes were used for masking the specimen with an exposure area of 1 mm^2. The corrosion potential and corrosion rate of the specimens in artificial seawater solution were analyzed through a potentiodynamic polarization test in an electrochemical workstation. The electrolyte for the test was prepared by adding 3.5 wt% of sodium chloride (NaCl) to distilled water. In the electrochemical cell setup, the test specimen was the working electrode, and the platinum rod was the counter electrode. The temperature was regulated using a thermostatic water bath setup. The potentiodynamic polarization test was carried out in the potential range of –1.5 V to –0.5 V. The generated Tafel plots were utilized to determine the corrosion current density, and the corrosion rates were calculated using equation (2) and equation (3).

$$i_{\text{corr}} = \frac{\beta_a \times \beta_c}{2.3 \times (\beta_a \times \beta_c)} \times \frac{1}{R_p} \quad (2)$$

$$\text{Corrosion Rate} = \frac{k \times i_{\text{corr}} \times E'}{A \times \rho} \quad (3)$$

where β_a is the slope of the anodic polarisation curve in Volts/decade, β_c is the slope of the cathodic polarisation curve in Volts/decade, R_p is polarization resistance in Ω (Ohms), k is constant, i_{corr} is corrosion current in Ampere, E' is equivalent weight in grams (g), A is the exposed area in cm^2 and ρ is the density of the material of the specimen in g cm^{-3}.

Characterization using advanced analytical instruments

The corroded specimens were preserved in a vacuum desiccator. The surface morphology of the specimens was captured using a field emission scanning electron microscope (SEM; Make: Zeiss Sigma; Model: Gemini 300). The elemental composition and distribution maps were obtained using energy dispersive X-ray spectroscopy (EDS; Make: Oxford Instruments; Model: Ultim Max) at an electron acceleration potential of 20 kV. A high-resolution transmission electron microscope (TEM; Make: Jeol; Model: JEM 2100) was utilized to examine the dislocations, sub-grain structures, and mechanically fragmented secondary phases in the specimen. Standard metallurgical preparation techniques and ion-beam etching were performed to prepare specimens for TEM analysis. Bright-field images, dark-field images, and selected area electron diffraction patterns were analyzed using CrystTBox analytical software.

RESULTS AND DISCUSSIONS

Macrostructure and defect analysis

The generation of thermal cycles largely influenced the defects in the specimens during FSP. The FSC materials were examined for macroscopic defects. The observed defects on the FSC materials are listed in Table 3. The poor plastic deformation and the material transport caused material penetration deficiency in specimen FSP01[20-23].

In FSP01 (single pass and double pass), the high TRS and low TTS led to the turbulent flow of the material. The high degree of plasticization during FSP occurred due to excess heat generation through frictional contact. Thus, surface lack of fill and scalloping were observed. In FSP02 (single pass and double pass), incorporation of high TRS led to high degree of plasticization because of excess heat generation. Thus, flash formation and scalloping were observed as defects on the FSPed material. In FSP03, high TTS caused poor heat input and a low degree of plasticization. This was because of low heat input attributed to the slow rate of tool traverse and hence ineffective material flow. The second pass was also performed, ensuring homogenous dispersion of the reinforcement particles. But, the formation of surface lack of fill and flash was eventually observed due to high plasticization. In FSP04, low TRS and medium TTS lead to effective material flow and moderate heat generation. Thus, FSP04 was the most suitable and optimized parameter for FSP.

Microstructure

The microstructure of the base material & FSC specimen FSP04 (stir zone) was observed using a scanning electron microscope coupled with an electron back scattered diffractometer. The EBSD maps were color-coded according to the inverse pole figures for the base material and FSC specimen, as shown in Figures 2 and 3, respectively. The colors represented the crystallographic orientation of the specimen. As seen in Figure 2a and

Tab. 3. Observation of the defects in FSP fabricated surface composite AA5083-CeO_2

Sl. No.	Specimen No.	Fabricated surface composite	Defects	Reason
1.	FSP01 (1 pass)	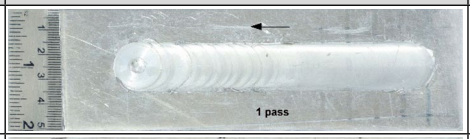	Surface lack of fill Scalloping	Inadequate heat generation and poor plastic deformation
2.	FSP01 (1 pass & 2 pass)	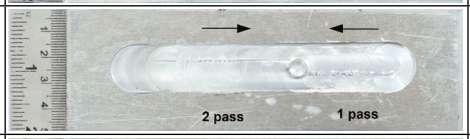	Flash Scalloping	High heat input and turbulent flow of material (2 passes)
3.	FSP02 (1 pass & 2 pass)	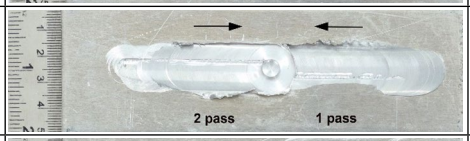	Flash Scalloping Surface lack of fill	High heat input and turbulent flow of material (2 passes)
4.	FSP03 (1 pass & 2 pass)	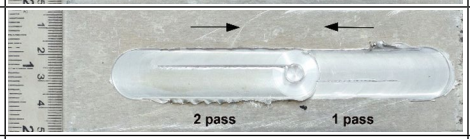	Flash Scalloping Surface lack of fill	High heat input and turbulent flow of material (2 passes)
5.	FSP04 (1 pass)	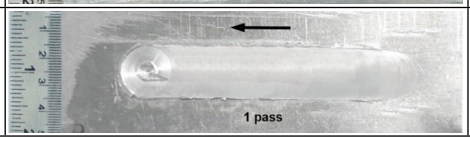	No Defects	Proper Parameters

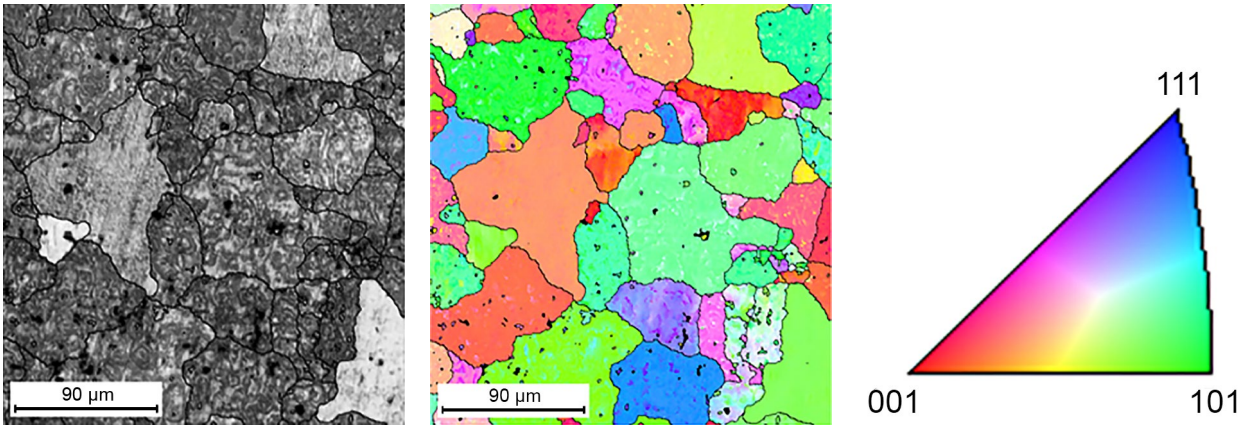

Fig. 2. Microstructure (a); Grain orientation map (b); Grain misorientation map (c) of the base material

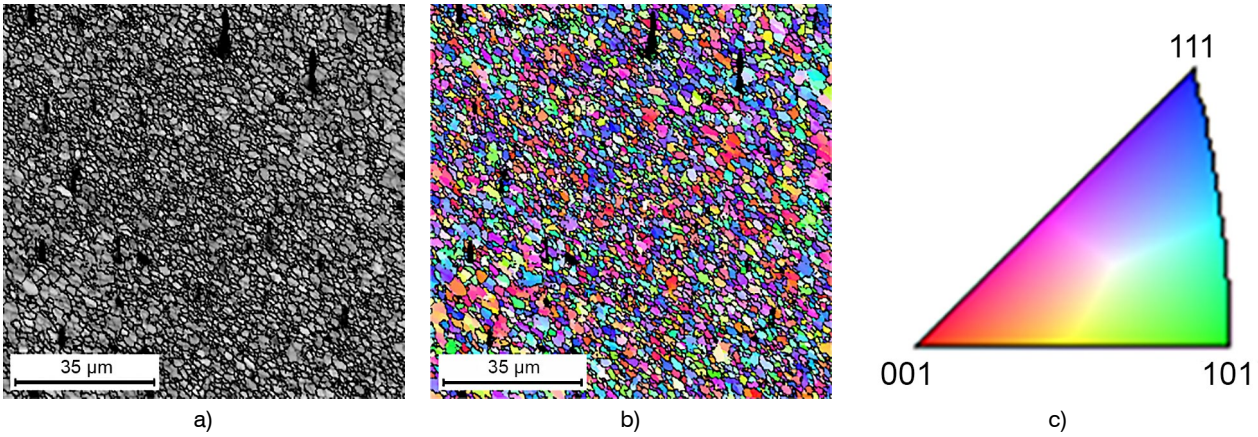

Fig. 3. Microstructure (a); Grain orientation map (b); Grain misorientation map (c) of the FSC specimen FSP04

Figure 3a, the base material consisted of coarse grains, whereas and FSC specimen consisted of recrystallized fine grains.

Around 50 % of the area fraction of base material had a grain size above 50 µm, and around 50% of the area fraction of Fabricated surface composite material had a grain size diameter below 2 µm. This inferred that the base material had coarse grains. Also, there was a formation of fine grains in the FSC specimen resulting from dynamic recrystallization in the course of FSP [21, 22, 24, 25]. The CeO_2 reinforcement particles acted as pinning agents and restricted the growth of recrystallized grains. Hence, the synergistic effect of FSP and CeO_2 reinforcement particles significantly reduced the grain size of the material [23].

A random orientation of the grains was observed in the base material and FSC specimen FSP04, as shown in Figures 2b and 3b. Each of the colors represents a specific direction of the crystal, as shown in Figures 2c and 3c. This indicated an absence of significant difference in the texture of both materials. About 50% of the number fraction of grains in the base material had a misorientation angle of less than 5º. About 50% of the fraction of grains in the FSC specimen FSP04 has a misorientation angle of less than 20º. However, about 90% of the number fraction of the grains in the FSC specimen FSP04 had grain orientation spread below 5º.

The crystallographic pole and inverse pole figures of the base material are shown in Figures 4 and 5, respectively. The pole figures in Figure 4 were interpreted by superimposing the standard stereographic projections for the crystallographic directions. As described earlier, no significant texturing effect was observed in the base material. Similarly, the FSC specimen FSP04 did not exhibit any significant characteristic texture, as shown in Figures 6 and 7, respectively.

Figure 8 shows the transmission electron microscopy of the FSC specimen. Figure 8a shows the thin thread-like structures, which depict the formation of subgrain structures (annihilated dislocations). Also, twist bands and partial dislocations were formed in Figure 8b. The cluster of dislocations, conventionally inferred to be the dislocation tangles [26], were perceived in Figure 8c. Figure 8d shows the dispersed and fragmented secondary phase and reinforcement particles in the grains of the FSC specimen.

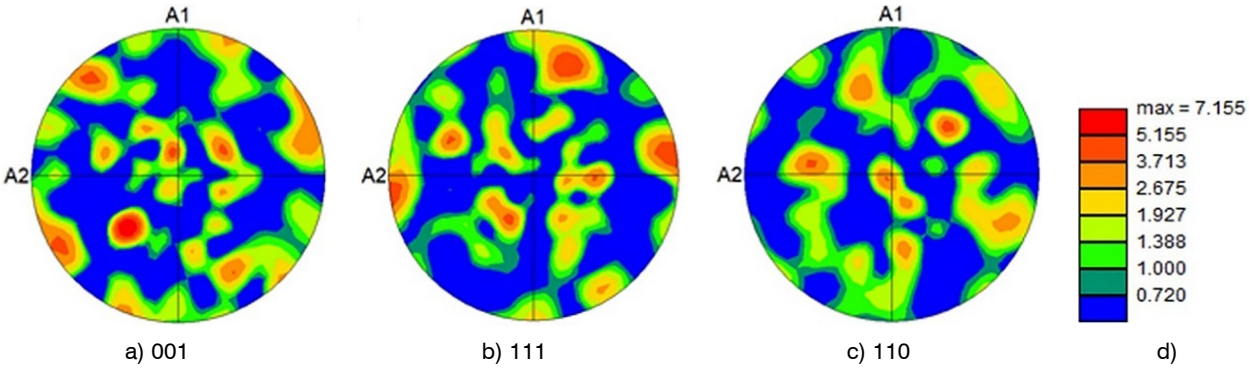

Fig. 4. Pole figure of the base material

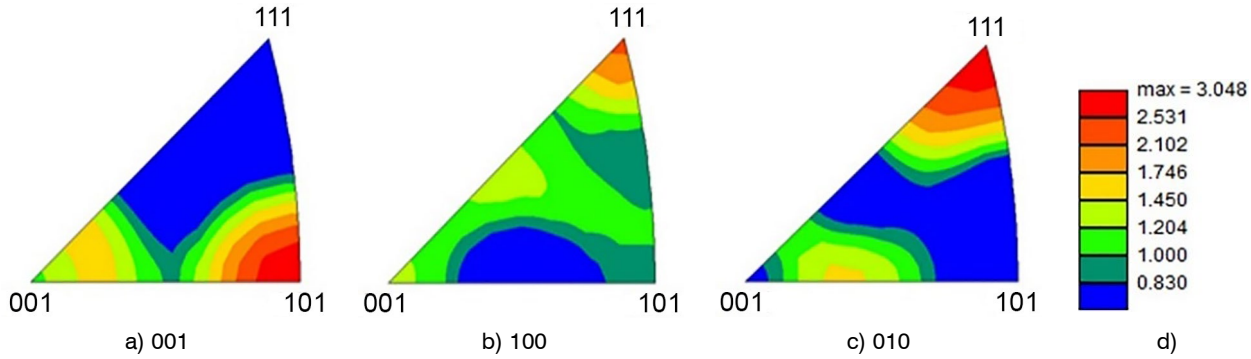

Fig. 5. Inverse pole figure of base material

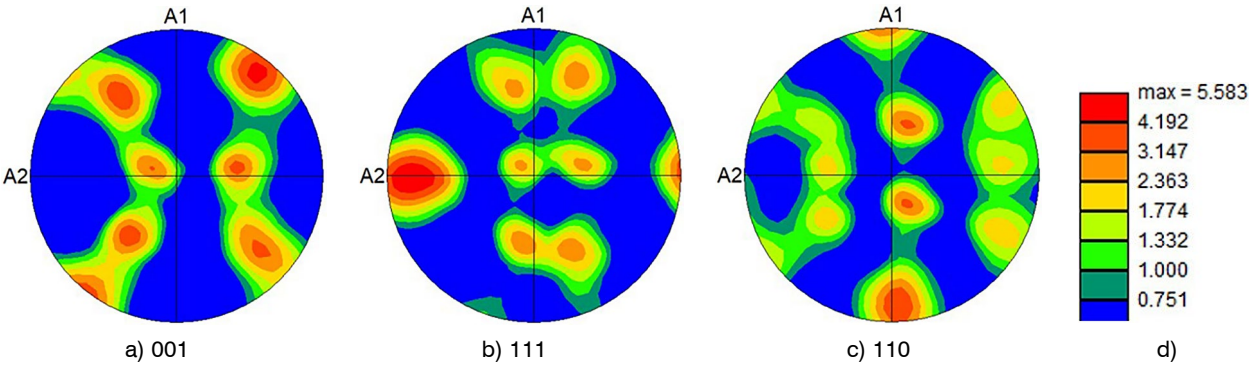

Fig. 6. Pole figure of the fabricated surface composite

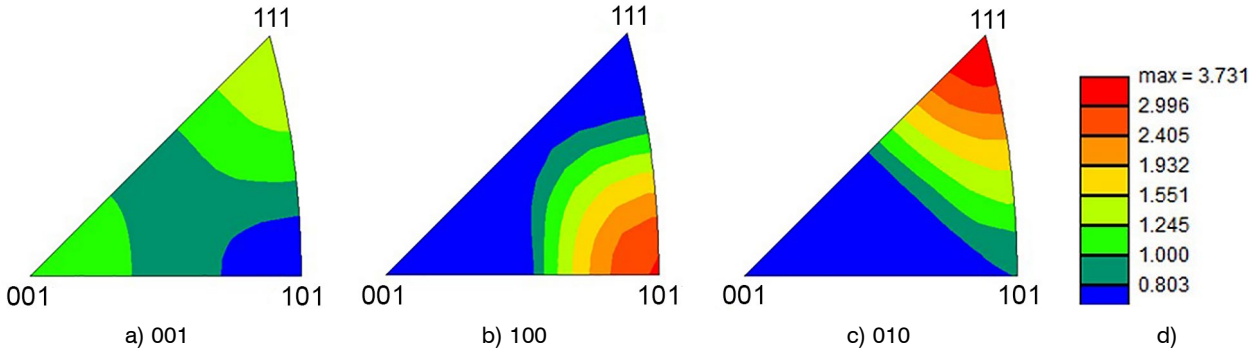

Fig. 7. Inverse pole figure of fabricated surface composite

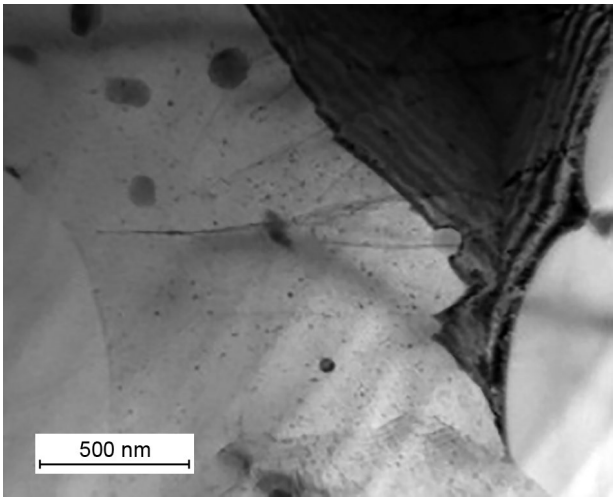

a)

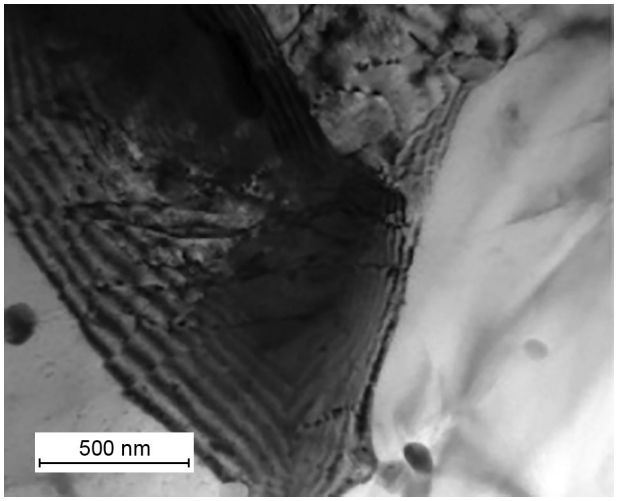

b)

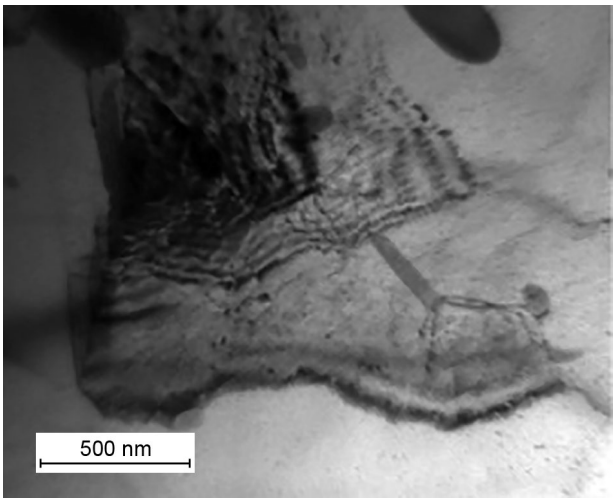

c)

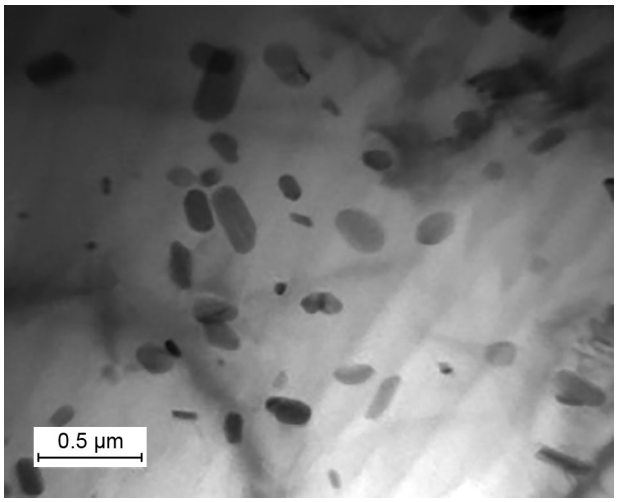

d)

Fig. 8. Sub grain structures (a); twist bands (b); dislocation tangles (c); dispersed particles (d) in the fabricated surface composite

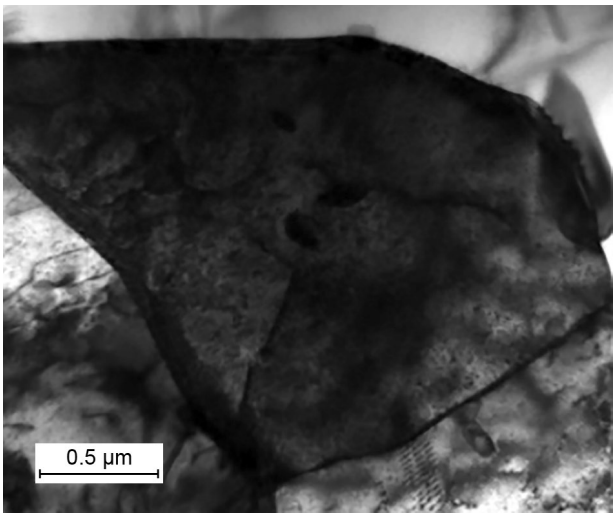

a)

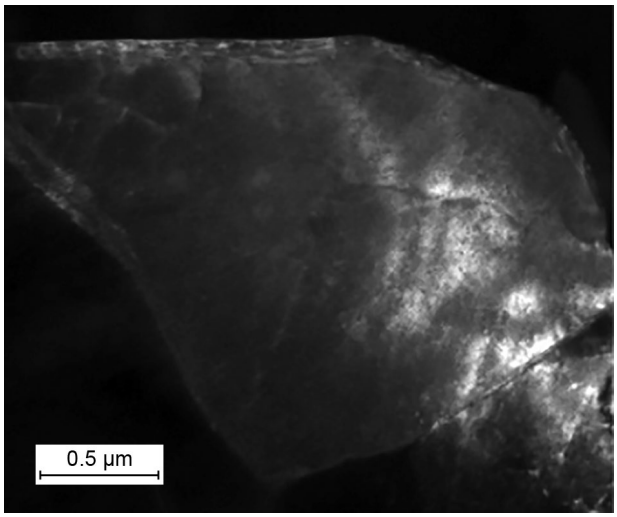

b)

Fig. 9. TEM micrograph showing the phase contrast in the fabricated surface composite: a) bright-field image; b) dark field image

The primary α phase was seen as bright regions and dark regions in Figures 9a and 9b in the bright field image and dark field image, respectively. The dark region in the bright field image was the β phases or the reinforcement particles. Also, there was no indication of the segregation of the secondary phase particles along the grain boundaries. Figure 10 shows the SAED pattern of the FSC specimen FSP04. The spot pattern formed confirmed the presence of α-Al and CeO_2 in the composite [27].

The phase composition analysis of the base material and FSC specimen is shown in Figure 11. α-Al, β-(Mg_2Al_3), Al–Mn phases were observed in the base material. The FSC specimen had α-Al, β-(Mg_2Al_3), Al–Mn phases, and CeO_2.

Microhardness

The microhardness of the specimens was obtained from the Vickers microhardness tester for the base material and the FSC specimen. The base material had an average hardness of 88 HV, whereas the FSC specimen had an average hardness of 122.0 HV. The hardness of the FSC specimen was 39% higher than the base material. The increase in hardness was attributed to the refined grain size in the stir zone of the FSC specimen [28]. Also, the presence of a homogeneous distribution of reinforcement particles increased the resistance of the material to localized plastic deformation. Furthermore, the formation of strain-free grains by dynamic recrystallization during FSP improved the hardness at the thermo-mechanically affected zone [29].

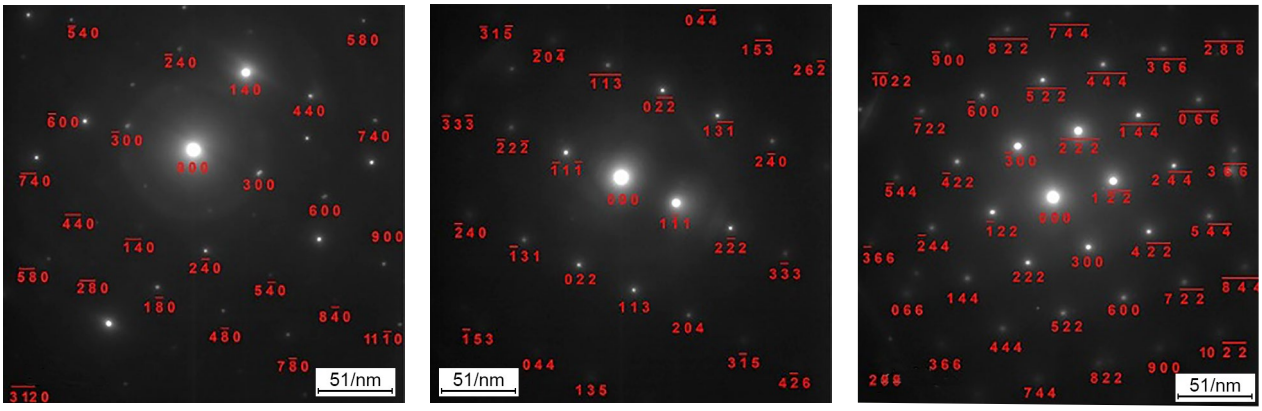

Fig. 10. Selected area electron diffraction pattern confirming the presence of: a) CeO_2; b) Al; c) Al in the fabricated surface composite

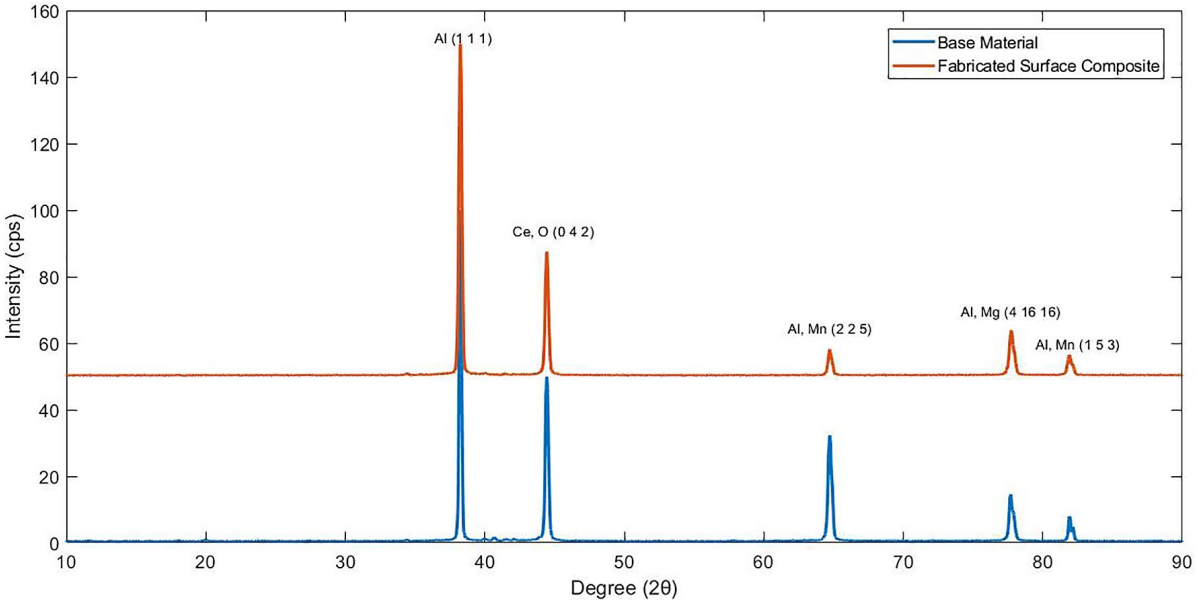

Fig. 11. XRD result of base & fabricated surface composite specimens

Intergranular corrosion susceptibility test

The IGC susceptibility of the base material and FSC specimen was investigated by performing the NAMLT test. During the IGC susceptibility test, the HNO_3 preferentially dissolves the intermetallic β-Mg_2Al_3 phase. In the eventuality of the β-phase segregated along the grain boundaries, immersion in HNO_3 would result in the shedding of the α-Al phase from the alloy matrix, causing huge mass loss. As per the ASTM standard, a mass loss between 25 mg/cm^2 and 75 mg/cm^2 would be observed in the specimens prone to IGC. If the alloy matrix had a fine dispersion of the β phase, an intermediate-mass loss between 15 mg/cm^2 and 25 mg/cm^2 would be observed [30]. The dissolution of agglomerated β phase causes the non-shedding of α grains from the matrix. Hence, IGC-resistant material will have less mass loss (typically less than 15 mg/cm^2). From the intergranular corrosion

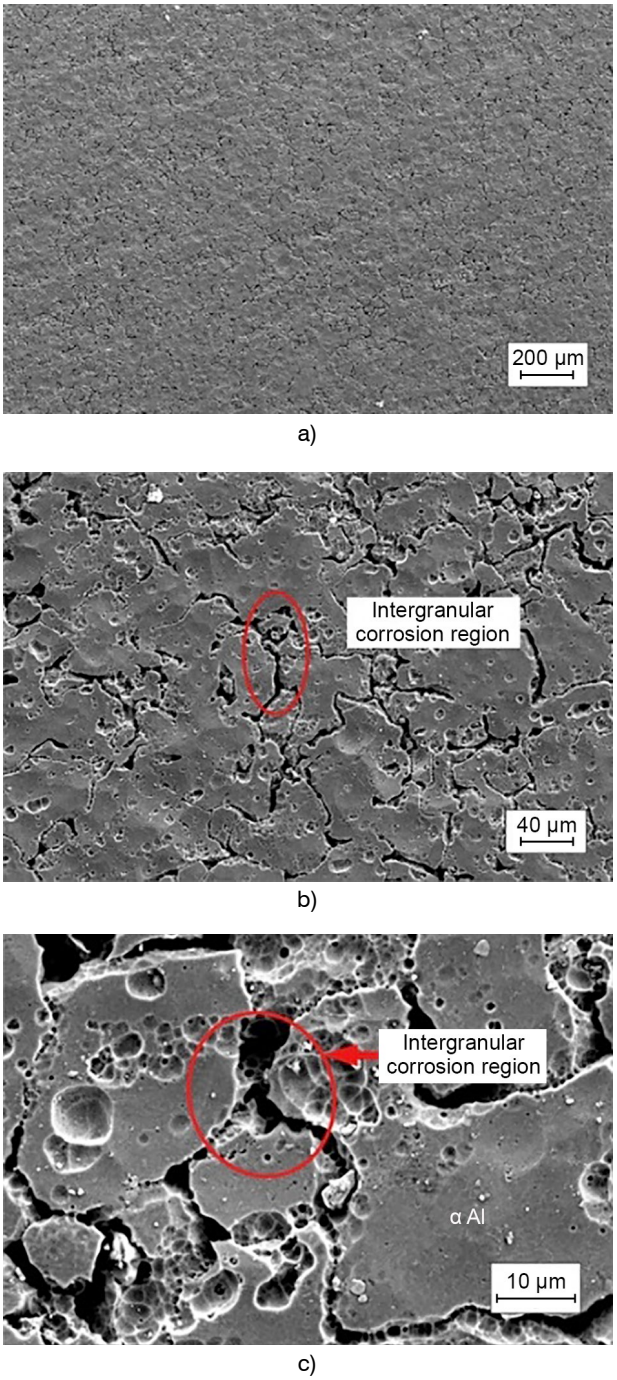

Fig. 12. Base material after IGC test at a magnification of: a) 50×; b) 250×; c) 1500×

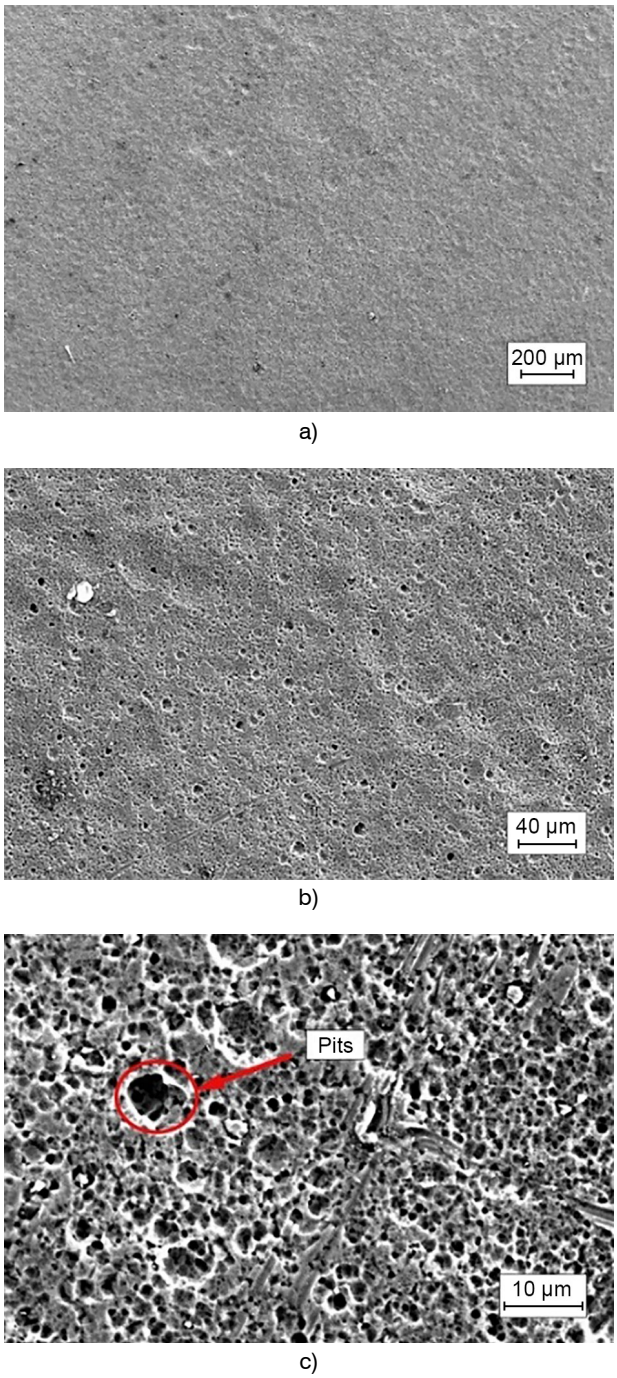

Fig. 13. FSC specimen after IGC test at a magnification of: a) 50×; b) 250×; c) 1500×

test, an intermediate-mass loss of ~3.7 mg/cm^2 was observed for the base material. And the FSC specimen had a mass loss of ~2.5 mg/cm^2. Hence, the IGC resistance of the FSC specimen was ~30% higher than in the base material.

Figures 12a-c provides a visual representation of the surface morphology of an AA5083 alloy after the NAMLT process, showcasing the microstructural features and characteristics of the surface. The results demonstrate that the base material, AA5083 alloy, was significantly impacted by intergranular corrosion (IGC). Intergranular corrosion refers to the corrosion that occurs specifically along the grain boundaries of a material. In this case, intergranular corrosion was visibly apparent even at relatively low magnification. The boundaries between adjacent grains exhibited signs of localized corrosion, indicating the occurrence of IGC. As the magnification increased, IGC regions became even more pronounced and distinguishable. Figure 12c details the extent and distribution of the intergranular corrosion in the alloy. The primary factor contributing to intergranular corrosion is the dissolution of the β phase particles. The particles were the localized corrosion sites, leading to the initiation and propagation of corrosion along their surfaces.

Figure 13 depicts the surface morphology of the FSC specimen after the IGC test. Upon careful examination of Figures 13a-c, limited indications of IGC occurrence were observed. The absence of IGC was attributed to two key factors that contributed to the corrosion resistance of the specimen FSC. Firstly, the β phase particles within the alloy matrix. Because β phase particles had undergone dissolution and fine dispersion in the course of FSP. As a result, the formation of localized corrosion sites along the grain boundaries was effectively inhibited, mitigating the risk of IGC. Secondly, the presence of CeO_2 particles contributed to the corrosion resistance observed in Figure 13. CeO_2 particles are known for their ability to act as corrosion inhibitors. The dispersed CeO_2 particles within the alloy matrix created a protective barrier that shielded the grain boundaries from corrosive environments. By impeding the access of corrosive agents to the vulnerable areas along the grain boundaries, the CeO_2 particles effectively suppressed the occurrence of intergranular corrosion.

Electrochemical corrosion analysis

The electrochemical corrosion test used the electrochemical cell setup mentioned in the Materials & Methods section. On the surface of the specimen, an anodic reaction produced Al^{3+} ions, as given in equation (4). Also, the cathodic reaction in the marine environment during the corrosion of the specimen caused the reduction of dissolved oxygen, leading to the formation of OH^- ions, as given by equation (5).

$$Al \rightarrow Al^{3+} + 3e^- \quad (4)$$

$$O_2 + 2H_2O + 4e^- \rightarrow 4OH^- \quad (5)$$

Due to the limited supply of reacting species, the cathodic limiting current was reached. In this case, the reacting species was considered as dissolved oxygen. Due to the inward diffusion of negative chloride ions and outward diffusion of positive aluminum ions, ionic charge neutrality was processed in the aluminum pit corrosion region in chloride environments. Aluminum ions undergo hydrolysis reaction with water, as given by any one of the equations (6) or (7) (North and MacLeod, 1987)

$$Al^{3+} + H_2O \rightarrow Al(OH)_2^+ + 2H^+ \quad (6)$$

$$Al^{3+} + H_2O \rightarrow Al(OH)_2^+ + H^+ \quad (7)$$

The formation of aluminum chloride species by the inward motion of the chloride ions, which was caused by high chloride ion concentration in the pits, is described in equation (8) to (10). Aluminum hydroxide species were transformed into $Al(OH)_2Cl$ in the presence of Cl ion, as given by equation (7) and equation (8). Hydrolysis of $Al(OH)_2Cl^+$ yields an unstable compound, which on further reaction with Cl, forms $AlCl_3$, as given by the equation (10).

$$Al(OH)_2^+ + Cl \rightarrow Al(OH)Cl^+ \quad (8)$$

$$Al(OH)Cl^+ + H_2O \rightarrow Al(OH)_2Cl + H^+ \quad (9)$$

$$2Al(OH)_2Cl + 4Na^+ + 4Cl^- \rightarrow 2AlCl_3 + 4NaOH \quad (10)$$

Calculation of corrosion potential, corrosion current, and corrosion rate

The difference between the E_{corr} of the base material and the specimen FSC tested at room (27 °C) temperature was observed to be very small. Corrosion current density was calculated from the anodic and cathodic Tafel constants using equation (1).

The corrosion rate of both specimens was calculated using equation (2). It was observed that the corrosion rate of the base material was 0.0501 (mm/year) at an equilibrium potential of –0.506, whereas the FSC had a corrosion rate of 0.0106(mm/year) at an equilibrium potential of –0.510 V. The corrosion rate of the fabricated surface composite was 68% lower than the base material.

CONCLUSION

Friction stir processing was successfully applied to the fabricated AA5083 alloy reinforced with CeO_2. The microstructural evolution, grain orientation, intergranular corrosion, and corrosion characteristics of the fabricated surface composite were examined. The results demonstrated the following:

- The optimal friction stir processing parameters for the fabrication of surface composite with homogeneous dispersion of CeO_2 particles was at low TRS of 350 rpm and medium TTS of 20 mm/min
- Around 50% of the area fraction of fabricated surface composite specimen had an average grain size of 2 µm compared to base material being above 50 µm. The formation of refined grains with homogeneous dispersion of the β phase was attributed to the pinning effect of CeO_2 particles and the dynamic recrystallization phenomenon. The hardness value of the FSC Specimen (122 HV) had increased by 39% compared to the base material.
- The mass loss was reduced by 30% in the fabricated surface composite specimen to the base material in the intergranular corrosion test. The fine dispersion of reinforcement particles and non-dissolution of submicron β phase particles attributed to the intergranular corrosion resistance of the fabricated surface composite
- The corrosion rate of the fabricated surface composite specimen was 0.0106 (mm/year) at an equilibrium potential of –0.510 V compared to the base material. The corrosion rate of the fabricated surface composite was 68% lower than the base material.

Cumulatively, the results suggest that friction stir processing and reinforcement of CeO_2 refined the grains and augmented the corrosion resistance (intergranular and electrochemical) of AA5083 alloy. Hence, CeO_2 could be suggested as a potential reinforcement for suppressing the corrosion of AA5083 alloy in marine environments.

REFERENCES:

1. Rasouli, S.; Behnagh, R. A.; Dadvand, A.; Saleki-Haselghoubi, N., Improvement in corrosion resistance of 5083 aluminum alloy via friction stir processing. *Proceedings of the Institution of Mechanical Engineers, Part L: Journal of Materials: Design and Applications* **2016,** *230* (1), 142-150.
2. Moldovan, P.; Stanica, C. N.; Ciobanu, G.; Ungureanu, I.; Iorga, G. M.; Buţu, M., Intergranular corrosion of AA 5083-H321 aluminum alloy. *UPB Sci Bull Ser B* **2014,** *76* (3), 169-80.
3. Amra, M.; Ranjbar, K.; Dehmolaei, R., Mechanical properties and corrosion behavior of CeO_2 and SiC incorporated Al5083 alloy surface composites. *Journal of Materials Engineering and Performance* **2015,** *24*, 3169-3179.
4. Huang, C.; Wu, Z.; Huang, R.; Wang, W.; Li, L., Mechanical Properties of AA5083 in Different Tempers at Low Temperatures, IOP Conf. *Series: Materials Science and Engineering* **2017**, 279.
5. Vignesh, R. V.; Padmanaban, R., Intergranular corrosion susceptibility of friction stir processed aluminium alloy 5083. *Materials today: proceedings* **2018,** *5* (8), 16443-16452.
6. Prabhakar, G.; Kumar, N. R.; Sunil, B. R., Surface metal matrix composites of Al5083-fly ash produced by friction stir processing. *Materials Today: Proceedings* **2018,** *5* (2), 8391-8397.
7. Jain, V. K. S.; Yazar, K.; Muthukumaran, S., Development and characterization of Al5083-CNTs/SiC composites via friction stir processing. *Journal of Alloys and Compounds* **2019,** *798*, 82-92.
8. Behnagh, R. A.; Shen, N.; Abdollahi, M.; Ding, H., Ultra-fine-grained surface layer formation of aluminum alloy 5083 by friction stir processing. *Procedia CIRP* **2016,** *45*, 243-246.
9. Ashraf, P. M.; Shibli, S., Reinforcing aluminium with cerium oxide: A new and effective technique to prevent corrosion in marine environments. *Electrochemistry Communications* **2007,** *9* (3), 443-448.
10. Jain, V. K.; Yadav, M. K.; Saxena, A.; Siddiquee, A. N.; Khan, Z. A., Effect of tool rotational speed on microstructure and mechanical properties of friction stir processed AA5083/Fe-Al in-situ composite. *Materials Today: Proceedings* **2021,** *46*, 6496-6500.
11. El-Danaf, E. A.; El-Rayes, M. M.; Soliman, M. S., Friction stir processing: an effective technique to refine grain structure and enhance ductility. *Materials & Design* **2010,** *31* (3), 1231-1236.
12. Huang, K.-T.; Lui, T.-S.; Chen, L.-H., Effect of microstructural feature on the tensile properties and vibration fracture resistance of friction stirred 5083 Alloy. *Journal of alloys and compounds* **2011,** *509* (27), 7466-7472.
13. García-Bernal, M.; Mishra, R.; Hernández-Silva, D.; Sauce-Rangel, V., Microstructural homogeneity and hot deformation of various friction-stir-processed 5083 Al Alloys. *Journal of Materials Engineering and Performance* **2017,** *26*, 460-464.
14. Hayashi, J.; Sarath Menon, E.; Su, J.; McNelley, T. R., Friction stir processing (FSP) of as-Cast AA5083 for grain refinement and superplasticity. *Key Engineering Materials* **2010,** *433*, 135-140.
15. Rahman, Z.; Siddiquee, A. N.; Khan, Z. A. In *Effect of Ti/SiC Reinforcement on AA5083 Surface Composites Prepared by Friction Stir Processing*, IOP Conference Series: Materials Science and Engineering, IOP Publishing: 2021; p 012001.
16. Zohoor, M.; Givi, M. B.; Salami, P., Effect of processing parameters on fabrication of Al–Mg/Cu composites via friction stir processing. *Materials & Design* **2012,** *39*, 358-365.
17. Amra, M.; Ranjbar, K.; Hosseini, S., Microstructure and wear performance of Al5083/CeO_2/SiC mono and hybrid surface composites fabricated by friction stir processing. *Transactions of Nonferrous Metals Society of China* **2018,** *28* (5), 866-878.
18. Jannet, S.; Raja, R.; Jaio, M. G.; Manohar, B., Synthesis and characterization of sic/Al_2O_3 reinforced aa5083 metal matrix composite by friction stir processing. *Int. J. Recent Technol. Eng* **2019,** *7*, 629-634.
19. Ikumapayi, O. M.; Akinlabi, E. T.; Pal, S. K.; Majumdar, J. D., A survey on reinforcements used in friction stir processing of aluminium metal matrix and hybrid composites. *Procedia Manufacturing* **2019,** *35*, 935-940.
20. Vaira Vignesh, R.; Padmanaban, R.; Datta, M., Influence of FSP on the microstructure, microhardness, intergranular corrosion susceptibility and wear resistance of AA5083 alloy. *Tribology-Materials, Surfaces & Interfaces* **2018,** *12* (3), 157-169.

21. Mishra, R. S.; Ma, Z., Friction stir welding and processing. *Materials science and engineering: R: reports* **2005,** *50* (1-2), 1-78.
22. Suganya Priyadharshini, G.; Satish Kumar, T.; Anbuchezhian, N.; Vaira Vignesh, R.; Subramanian, R.; Velmurugan, T.; Kamal Basha, K., Influence of tool traverse speed on microstructure and mechanical properties of CuNi/B4C surface composites. *Transactions of the IMF* **2021,** *99* (1), 38-45.
23. Węglowski, M. S., Friction stir processing – state of the art. *Archives of civil and Mechanical Engineering* **2018,** *18*, 114-129.
24. Han, J.; Paidar, M.; Vignesh, R. V.; Mehta, K. P.; Heidarzadeh, A.; Ojo, O., Effect of shoulder features during friction spot extrusion welding of 2024-T3 to 6061-T6 aluminium alloys. *Archives of Civil and Mechanical Engineering* **2020,** *20*, 1-17.
25. Samuel Ratna Kumar, P.; Vaira Vignesh, R.; Mashinini, P.; Ramanathan, S., Tribological behavior of friction stir process surface hybrid composite AA5083/MWCNT/Al_2SiO_5 using multi-quadratic RBF algorithm. *Carbon Letters* **2023**, 1-15.
26. Kurt, A.; Uygur, I.; Cete, E., Surface modification of aluminium by friction stir processing. *Journal of materials processing technology* **2011,** *211* (3), 313-317.
27. Luo, J.; Liu, S.; Paidar, M.; Vignesh, R. V.; Mehrez, S., Enhanced mechanical and tribological properties of AA6061/CeO2 composite fabricated by friction stir processing. *Materials Letters* **2022,** *318*, 132210.
28. Shahraki, S.; Khorasani, S.; Abdi Behnagh, R.; Fotouhi, Y.; Bisadi, H., Producing of AA5083/ZrO_2 nanocomposite by friction stir processing (FSP). *Metallurgical and Materials Transactions B* **2013,** *44*, 1546-1553.
29. Li, H.; Paidar, M.; Ojo, O. O.; Vignesh, R. V.; Iswandi, I.; Mehrez, S.; Zain, A. M.; Mohanavel, V., Effect of tool profile on wear and mechanical behaviors of CeO_2 and ZrO_2-reinforced hybrid magnesium matrix composite developed via FSP technique. *Journal of Manufacturing Processes* **2023,** *94*, 297-315.
30. Choi, D.-H.; Ahn, B.-W.; Quesnel, D. J.; Jung, S.-B., Behavior of β phase (Al3Mg2) in AA 5083 during friction stir welding. *Intermetallics* **2013,** *35*, 120-127.

DECLARATIONS

Funding

The authors and co-authors did not receive specific grant from any funding agency in the public, commercial, or not-for-profit sectors to carry out the research.

Conflicts of interest/Competing interests

The authors declare that there is no conflict of interest or competing interests for the research work.

Availability of data and material (data transparency)

All data generated or analysed during this study are included in this published article (and its supplementary information files).

Code availability

Not Applicable

Ethics approval

Not Applicable

Consent to participate

Not Applicable

Consent for publication

Not Applicable